ACS OMEGA

Open Access

http://pubs.acs.org/journal/acsodf

Article

Theoretical Investigation of the Green-Synthesized Carbon-Based Nanomaterial Potential as Inhibitors of ACE2 for Blocking SARS-CoV-2 Binding

Harsiwi Candra Sari, Haliza Hasnia Putri, Pinantun Wiguna Kusuma Paksi, Gabriel Hidayat, Silmi Rahma Amelia, Citra Deliana Dewi Sundari, Heni Rachmawati, Atthar Luqman Ivansyah,* Fahdzi Muttaqien,* and Ferry Iskandar*

Cite This: *ACS Omega* 2024, 9, 16701−16715

Read Online

ACCESS | Metrics & More | Article Recommendations

ABSTRACT: Since the emergence of SARS-CoV-2 in 2020, the world has faced a global pandemic, emphasizing the urgent need for effective treatments to combat COVID-19. This study explores the use of green-synthesized carbon-based nanomaterials as potential inhibitors of ACE2, a critical receptor for SARS-CoV-2 entry into host cells. Specifically, the study examines four carbon-based nanomaterials, namely, CD1, CD2, CD3, and CD4 in amino, graphitic, pyridinic, and pyrrolic forms, respectively, synthesized from curcumin, to investigate their binding affinity with ACE2. Molecular docking studies revealed that CD3 (pyridinic form) exhibited the highest binding affinity with ACE2, surpassing that of the control compound, curcumin. Notably, CD3 formed hydrophobic interactions and hydrogen bonds with key ACE2 residues, suggesting its potential to block the binding of SARS-CoV-2 to human cells. Moreover, molecular dynamics simulations demonstrated the stability of these ligand-ACE2 complexes, further supporting the promise of CD3 as an inhibitor. Quantum chemical analyses, including frontier molecular orbitals, natural bond orbital analysis, and the quantum theory of atoms in molecules, unveiled valuable insights into the reactivity and interaction strengths of these ligands. CD3 exhibited desirable chemical properties, signifying its suitability for therapeutic development. The study's findings suggest that green-synthesized carbon-based nanomaterials, particularly CD3, have the potential to serve as effective inhibitors of ACE2, offering a promising avenue for the development of treatments against COVID-19. Further experimental validation is warranted to advance these findings and establish new therapies for the ongoing global pandemic.

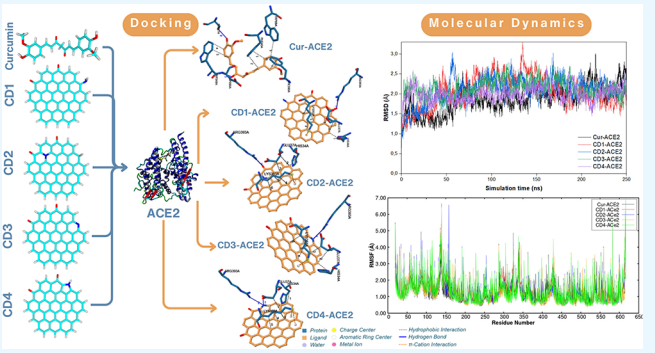

1. INTRODUCTION

SARS-CoV-2, the cause of COVID-19, has plagued almost all countries worldwide since early 2020. The global outbreak of the virus began with reports of pneumonia cases in Wuhan City, Hubei Province, China, and was designated a pandemic by the World Health Organization (WHO) on March 11, 2020.[1] Infections caused by the virus in humans cause various types of bodily responses.[2] Some of these patients are asymptomatic; however, there are also cases in which they show early symptoms. The most common symptoms are fever, dry cough, stuffy nose, runny nose, and sore throat. Eighty percent of people who experience these symptoms recover without requiring special treatment.[3] But in some people, it can cause serious illnesses. If the infection is not treated immediately, the body's condition will worsen; therefore, it is not uncommon for patients to receive special treatment, such as mechanical ventilation or extracorporeal membrane oxygenation.[4,5]

The negative impact of SARS-CoV-2 is accompanied by its ability to mutate rapidly.[6] There are five variants of SARS-CoV-2 that are of major concern: alpha (B.1.1.7), beta (B.1.351), gamma (P.1), delta (B.1.617.2), and Omicron (B. B.1.1.529).[7,8] Of the five variants, the Omicron variant is the most recently discovered, namely, in November 2021 in South Africa.[9,10] Mutations that occur in the omicron variant in the receptor binding domain (RBD) area are G339D, S371L,

Received: January 23, 2024
Revised: March 1, 2024
Accepted: March 12, 2024
Published: March 27, 2024

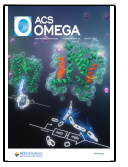

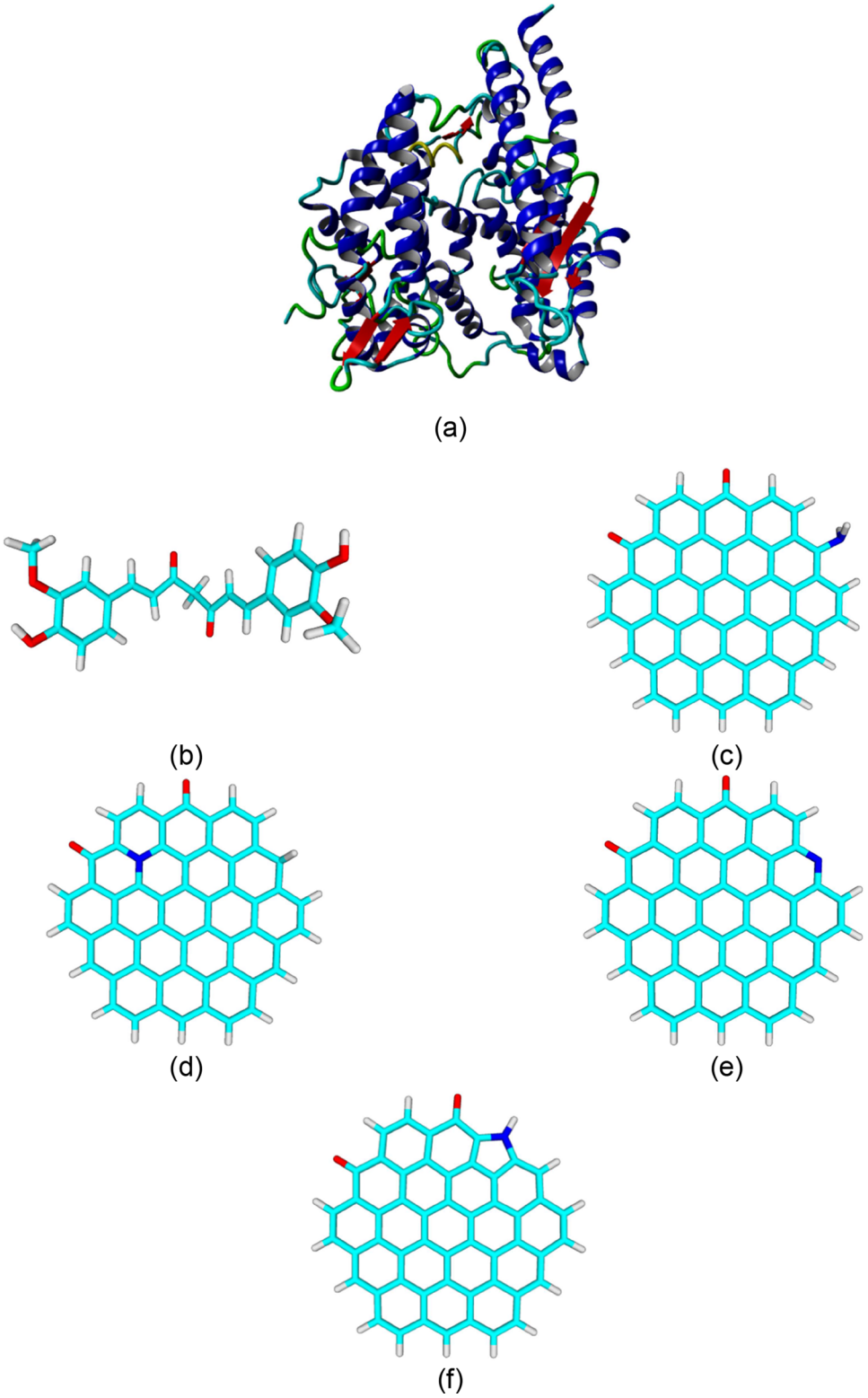

Figure 1. Structure of (a) angiostensin converting enzyme 2 (ACE2), (b) curcumin (CUR), (c) carbon dot in amino form (CD1), (d) carbon dot in graphitic form (CD2), (e) carbon dot in pyridinic form (CD3), and (f) carbon dot in pyrrolic form (CD4).

S373P, S375F, K417N, N440 K, G446S, S477N, T478 K, E484A, Q493R, G496S, Q498R, N501Y, and Y505H.[11,12] The RBD contained in protein S (spike protein) plays an important role in the infection process.[13] This protein has a strong affinity for the angiotensin-converting enzyme 2 (ACE2) receptor in humans, which is an enzyme found in the cell membranes of the respiratory tract, stomach, small intestine, large intestine, kidney, lymph nodes, and bile ducts.[14,15] Therefore, this enzyme is considered as the main entry point for SARS-CoV-2.[15]

One method that can be used to minimize the impact of infection by SARS-CoV-2, especially the omicron variant, is to

https://doi.org/10.1021/acsomega.4c00759
ACS Omega 2024, 9, 16701−16715

use a vaccine. As of January 20, 2022, 60.20% of the world's population had been vaccinated.[16] In Indonesia, 122.4 million people have received the second dose of vaccine, and at least 179.2 million people have received the first dose of vaccine.[17] Although most of the global population has been vaccinated, mutations that cause the SARS-CoV-2 virus to experience partial resistance to the vaccine can take a longer time to achieve herd immunity.[18] Therefore, it is necessary to develop drugs as an effective alternative to prevent the COVID-19 infection. Several drugs have inhibitory activity against the SARS-CoV-2 virus, including remdesivir, chloroquine, and lopinavir.[19,20] These drugs have different inhibitory schemes. The target of remdesivir inhibition is to inhibit RNA-dependent RNA polymerase (RdRP) RNA viruses, which in this case include SARS-CoV-2. This inhibition can lead to premature termination of the virus.[21] In contrast to remdesivir, chloroquine acts at the entry and postentry stages of the virus and can interfere with the glycosylation of the SARS-CoV-2 cell receptor.[22] The drug lopinavir can act as a major proteinase inhibitor of the coronavirus, thereby interfering with the processing of polypeptide translation products.[23] Even so, these drugs can have a negative impact on the body if consumed in the long term. The side effects include nausea, hypokalemia, headache, indigestion, and cardiomyopathy (hypertrophy and heart failure).[24−26] The many side effects caused by these drugs encourage researchers to obtain inhibitors with minimal side effects or with lower levels of toxicity.

An option for replacing these medications involves the utilization of carbon-based nanomaterials. This material's versatility is rooted in its capacity to establish connections with a wide range of bonds differing in type and strength, whether composed of the same element (carbon) or other elements. Additionally, carbon can undergo hybridization in sp, sp^2, and sp^3 arrangements, creating possibilities for generating various allotropes.[27,28] In nature, two carbon allotropes exist: diamond and graphite.[29] In addition, other allotropes have been synthesized and utilized in biomedicine such as graphene quantum dots (GQDs). This material has attracted the interest of several research groups because it has several unique properties, such as a high surface area (2630 m^2/g) and high thermal, optical, and catalytic characteristics.[30,31] In addition, this material has high electrical conductivity, which is influenced by the high electron transport ability due to quantum confinement and edge effects.[32] This high electron movement can cause a reaction to occur with fast intensity so that GQDs can be applied as a good sensor. Moreover, this material is chemically stable, exhibits low toxicity, and exhibits strong fluorescence.[33] As a result, apart from being sensors, GQDs can be used for bioimaging and targeted drug delivery, which is supported by their ability to dissolve in water-based solvents.[34]

In the manufacturing process, the synthesis of GQDs is the same as that of other carbon-based materials, which is conventionally performed using fossil raw materials such as oil and coal. This synthesis process requires a high-energy route and complex conditions at each stage of synthesis.[35] In addition, the use of these raw materials is starting to be considered because they are nonrenewable, limited in availability, and very expensive. This has prompted researchers in recent years to synthesize carbon-based materials with green synthesis pathways that are renewable, low cost, biodegradable, and abundantly available.[32] One of the natural ingredients can be used in the synthesis of carbon-based materials. This compound belongs to a group of polyphenolic compounds that can be found in turmeric (*Curcuma longa* L.). Its use in the health sector is based on its biofunctional properties, such as antitumor, antioxidant, and anti-inflammatory properties.[36]

Lin et al. showed that curcumin-derived quantum dots (Cur-QDs) synthesized through a simple dry-heating treatment of curcumin can be used as an inhibitor of enterovirus 71 (EV71), with the inhibition process occurring during the replication process.[37] In 2022, Chen et al. succeeded in showing that Cur-QDs have antiviral abilities against Japanese encephalitis virus (JEV).[38] In this study, Cur-QDs were able to bind directly to the E-S123/K312 site of the JEV protein, which inhibited the binding of the virus to the host cell.

However, the two viruses mentioned above are included in the type of RNA virus, the same type as the virus that has become the current global epidemic, SARS-CoV-2. Thus, the focus of this study was to investigate the ability of four predictive compounds from green synthesis with curcumin (GQDs in amino, graphitic, pyridinic, and pyrrolic forms) in blocking the binding of RBD to the ACE2 receptor in host cells. In particular, the antiviral ability of GQDs was identified in this study by measuring the binding affinity and in silico analysis using molecular docking techniques. The inhibitory ability of these compounds was also calculated by using density functional theory (DFT) and molecular dynamics (MD) simulations. The results of this investigation may provide rich insights for further validation by experimental researchers and for the development of new therapies for COVID-19.

2. COMPUTATIONAL DETAILS

The first step in this study was the preparation of the structure of the ligand and protein compounds. As of this step, the ACE2 receptor crystal structure in PDB file format was retrieved from the RSCB PDB database (https://www.rscb.org). Code 6M0J, chain A, for the examined structure is shown in Figure 1a.[39] For ligand preparation, the structure of curcumin was obtained from the PubChem database in Sybil Data Files (sdf) format,[40] while the structures of the other ligands were modeled using Avogadro software (1.2.0),[41] as shown in Figure 1b−f.

The next stage is sterilization of the 3D structure of the protein compound with the aim of removing the water content and all ligands contained in the ACE2 receptor compound. After sterilization, the molecular docking and molecular dynamics process was carried out using the YASARA software version 19.5.5.[42] This process aims to identify the structures of ligands that are potential candidates for inhibiting the binding of the RBD protein SARS-CoV-2 against the ACE2 receptor. Furthermore, visualization of the interactions that have been identified was used to determine the distance of the bond, the type of bond, and the amino acids involved in the ligand-protein interaction.

Molecular orbital calculations were then performed on the docked complexes using ORCA 4.2.0[43,44] All structures were optimized using density functional theory (DFT) at the B3LYP functional with the def2-TZVP basis set[45−48] Reactivity parameter calculation is carried out using Koopman Theory with these eqs 1−4.[49]

$$\mu = \frac{(E(\mathrm{LUMO}) + E(\mathrm{HOMO}))}{2} \quad (1)$$

https://doi.org/10.1021/acsomega.4c00759
ACS Omega 2024, 9, 16701−16715

$$\eta = \frac{(E(\mathrm{LUMO}) - (E(\mathrm{HOMO}))}{2} \quad (2)$$

$$S = \frac{1}{\eta} \quad (3)$$

$$\omega = \frac{\mu^2}{2 \times \eta} \quad (4)$$

The symbols employed in this context include μ to denote the chemical potential, η representing the chemical hardness, S signifying the global softness, ω indicating the electrophilicity index, and HOMO−LUMO referring to the highest and lowest molecular orbitals, respectively. Additionally, the analysis encompassed the evaluation of second-order energy perturbation ($E^{(2)}$) within the framework of the natural bond orbital (NBO) calculated by eq 5. This energy is associated with delocalization $i \rightarrow j$

$$E^{(2)} = \Delta E_y = q_i \frac{F_{ij}^2}{\varepsilon_j - \varepsilon_i} \quad (5)$$

where q_i represents the occupancy of the donor orbital at the ith position, ε_i and ε_j are the individual orbital energies indicated along the diagonal, and F_{ij} pertains to the off-diagonal Fock matrix element of NBO. To determine the noncovalent interaction between ligand and ACE2 system, noncovalent interaction−reduced density gradient (NCI−RDG) analysis was carried out by the eq 6. It is worth noting that RDG, a dimensionless fundamental parameter derived from electron density $\rho(r)$ and its initial derivative $\nabla\rho(r)$ (as outlined in eq 6), was initially formulated by Johnson and colleagues, as documented in the literature.

$$\mathrm{RDG}(r) = \frac{1}{2(3\pi^2)^{1/3}} \frac{\nabla\rho(r)}{\rho(r)^{4/3}} \quad (6)$$

The quantum theory of atoms in molecules (QTAIM) and assessments of NCI-RDG were visualized using VMD.[50−52] Furthermore, the NBO executed using the external software package NBO version 7.0, which was integrated into the Orca 4.2.0 program package.[53]

Identification of binding energy in ligand-ACE2 was conducted by molecular docking in YASARA. The empirical formula for determining the binding energy is given in eq 7.

$$\Delta G = \Delta G_{\mathrm{vdW}} + \Delta G_{\mathrm{Hbond}} + \Delta G_{\mathrm{elec}} + \Delta G_{\mathrm{tor}} + \Delta G_{\mathrm{desol}} \quad (7)$$

where ΔG_{vdW}, $\Delta G_{\mathrm{Hbond}}$, ΔG_{elec}, ΔG_{tor}, and $\Delta G_{\mathrm{desol}}$ are the free energy changes for van der Waals interactions, hydrogen bonds, electrostatic, torsional changes of the compound before and after forming an interaction, and desolvation of the compound, respectively. Furthermore, molecular dynamics (MD) simulations were performed to investigate the dynamic behavior of complexes and their conformational changes, as well as to investigate the stability of the predicted binding interactions between ligands and important residues of ACE. Root mean square deviations (RMSD) is a measurement of deviations in the protein or protein−ligand complex structure compared to a reference structure. RMSD calculated according to eq 8.

$$\mathrm{RMSD} = \sqrt{\frac{\sum_{i=1}^{n} R_i \times R_i}{n}} \quad (8)$$

R_i represents the vector connecting the locations of atom i out of N total atoms in the reference snapshot and the present snapshot following the ideal superimposition. Whereas, root mean square fluctuations (RMSF) is a dynamic parameter that measures residual flexibility in the side chains of a protein. The basis of the RMSF calculation is shown in eq 9.

$$\mathrm{RMSF} = \sqrt{\sum_{j=1}^{3} \left(\frac{1}{N}\right) \sum_{k=1}^{N} P_{ikj}^2 - P_{ij}^{-2}} \quad (9)$$

where i and j are atoms running from 1 to 3 for the x, y, and z coordinates of the atom position vectors P and k running over the set of N evaluated snapshots. The compactness of protein structure was described with radius of gyration (R_g) (eq 10),

$$\mathrm{Radius}_{\mathrm{gyr,mass}} = \sqrt{\frac{\sum_{i=1}^{N} \mathrm{Mass}_i (\vec{R}_i - \vec{C})^2}{\sum_{i=1}^{N} \mathrm{Mass}_i}} \quad (10)$$

where C is the center of mass and R_i is the position of atom i of N.

3. RESULTS AND DISCUSSION

3.1. Frontier Molecular Orbitals (FMOs) and Dipole Moment Analysis. In this study, the chemical reactivity of the analyzed molecule was described by a powerful model developed by Kenichi Fukui in 1952, named the frontier molecular orbitals (FMOs) theory.[54] At this stage, the FMOs can describe the electronic properties of all ligands by utilizing the highest occupied molecular orbital (HOMO)−lowest unoccupied molecular orbital (LUMO) energy. During molecular interactions, the HOMO represents electron donors and is related to the ionization potential (IP), whereas the LUMO represents the electron acceptor and is related to the electron affinity (EA).[55] Knowledge of the gap energies of these values, which is presented in Table 1, is very important in determining the chemical stability of the molecule. In addition, it was used to calculate chemical reactivity descriptors.

Drawing from existing research, it is evident that molecules characterized by a narrow HOMO−LUMO energy gap tend to display heightened chemical reactivity but reduced kinetic stability. Conversely, molecules featuring a wide HOMO−LUMO energy gap showcase a lower chemical reactivity while maintaining a greater kinetic stability. This divergence arises

Table 1. HOMO, LUMO, Gap Energy, and Dipole Moment of Ligands before and after Interaction with ACE2

system	HOMO (eV)	LUMO (eV)	gap energy (eV)	dipole moment (D)
curcumin	−5.870	−2.276	3.594	6.201
Cur−ACE2	−3.593	−3.103	0.018	31.156
CD1	−5.118	−3.641	1.477	8.092
CD1−ACE2	−5.535	−5.175	0.013	33.496
CD2	−4.563	−3.298	1.265	9.000
CD2−ACE2	−3.671	−3.435	0.009	47.953
CD3	−5.360	−3.775	1.585	9.991
CD3−ACE2	−3.941	−3.715	0.008	53.837
CD4	−5.046	−3.595	1.451	8.015
CD4−ACE2	−5.483	−5.056	0.016	37.259

https://doi.org/10.1021/acsomega.4c00759
ACS Omega 2024, 9, 16701−16715

from the fact that elevating electrons from the lowest energy state to the highest energy state is energetically unfavorable. In simpler terms, compounds endowed with a substantial HOMO−LUMO energy gap are associated with increased stability and enhanced chemical resistance compared with those with a narrower HOMO−LUMO energy gap.

As a result of this calculation, curcumin was found to have the largest energy gap (3.5944 eV). This is in line with the results of the chemical descriptor calculation, as shown in Table 2. From that table, curcumin has the highest hardness

Table 2. Chemical Potential, Chemical Hardness, Global Softness, and Electrophilicity Index

system	chemical potential (μ)	chemical hardness (η)	global softness (S)	electrophilicity index (ω)
curcumin	−4.073	1.797	0.557	4.616
Cur−ACE2	−3.348	0.009	111.111	622.840
CD1	−4.380	0.739	1.354	12.983
CD1−ACE2	−5.355	0.007	151.515	2172.345
CD2	−3.930	0.633	1.581	12.209
CD2−ACE2	−3.553	0.004	232.558	1467.885
CD3	−4.568	0.793	1.262	13.159
CD3−ACE2	−3.828	0.004	243.902	1787.116
CD4	−4.321	0.726	1.378	12.866
CD4−ACE2	−5.270	0.008	126.582	1757.645

level with a value of 1.797 eV and the lowest global softness with a value of 0.557 eV^{-1}. The hardness of this compound was also supported by its smallest dipole moment (6.201 D). These results indicated that curcumin was the most stable compound among the four ligands. In addition, the CD2 ligand had the lowest energy gap (1.265 eV). This result is also consistent with the data for the lowest hardness level (0.633 eV) and the highest softness level (123 eV). Based on this theory, molecules with large softness (σ) values are more reactive than molecules with small softness (σ) values. Thus, an effective molecule used as an ACE2 inhibitor is expected to have a low hardness (η) and high softness (σ) value. Therefore, the order of the reactivity of the ligands as ACE2 inhibitors was CD2 > CD4 > CD1 > CD3 > Curcumin.

Table 1 reveals a decline in the overall system's energy gap following the binding of the ligand to ACE2. This decrease can be attributed to the potent electron-accepting capabilities of the electron acceptor groups, consequently leading to charge transfer interactions in the examined compounds. Additionally, the electrophilicity index data provide insights into the system's reactivity and performance. Following the interaction of ligands with ACE2, it is observed that the electrophilicity index values for each system rise. This phenomenon suggests that the system retains its reactivity when it interacts with other ligand molecules.

3.2. Natural Bond Orbital Analysis. The application of NBO analysis offers a valuable means to explore the interaction dynamics between the primary occupied Lewis-type orbitals, such as lone pairs and π electrons of an atom, and the unoccupied non-Lewis-type orbitals, which include the antibonding orbitals of another atom. Additionally, this analytical approach supplies information about the nature of hybridization and the intensity of the interaction between the ligand and the receptor. Within the context of this research, NBO analysis was carried out to assess the energy strength associated with the donor−acceptor interaction, focusing on the analysis of second-order perturbation stabilization energies denoted as $E^{(2)}$.

The second-order perturbation energies computed within the NBO framework provide validation for the existence of intermolecular interactions, as documented in Table 3. In the complex between curcumin and the active pocket of ACE2, interaction occurs between lone pair electrons and the antibonding orbitals LP(3)O152 → π*(C205−H206), LP(1)-O200 → π*(C39−H40), and LP(1)O204 → π*(C149−H150) with stabilization energies of 0.31, 0.16, and 0.66 kcal/mol, respectively. Besides that, bonding orbitals also involved in intermolecular interaction in π(C17−C21) → π*(C182−H187), π(C69−H70) → π*(C182−C183), π(C102−H103) → π*(C174−H191), π(C182−H187) → π*(C17−C21), and π(C183−H188) → π*(C69−C70) with the stabilization energies of 0.330, 0.160, 0.120, 0.490, and 0.560 kcal/mol, respectively. From these data, the energy of the most stable interaction is just 0.660 kcal/mol. This low energy indicates that curcumin was not strong enough to inhibit the ACE2 activity.

A difference in the amount of stabilization energy was observed for the other ligand compounds. The most stable energy for each compound in the CD1, CD2, CD3, and CD4 cells was higher than that of curcumin. In the complex between CD1 and ACE2, electrons were transferred from the bonding orbital of CD1 to the antibonding orbital of unit 3 (Lys353) π(C153−H165) → π*(N73−H75) with a stabilization energy of 1.570 kcal/mol. The character of this interaction can also be seen in the interactions that occur between CD2, CD3, and CD4 with ACE2, where the bonding orbitals of the ligands interact with the antibonding orbitals of the hydrogen-bonded acceptor (π*N−H) in unit 3 (Lys353). The electrons were transferred from the bonding orbital of the ligands to the antibonding orbital of ACE2, with stabilization energies of 2.300, 2.110, and 2.670 kcal/mol, respectively. These energies were higher than the energy in the curcumin-ACE2 complex, revealing that all ligand samples had a stronger interaction with ACE2 in the order CD4 > CD2 > CD3 > CD1 > Cur.

3.3. Quantum Theory Atoms in Molecule Analysis. In 1990, Bader introduced the QTAIM as a valuable instrument for extracting insights into the bonding characteristics of systems by studying the electron density topology. This method unveils both covalent and noncovalent interactions existing within a molecular system. Following Bader's theory, each pair of interacting atoms is connected by a bond path (BP), and a specific point (saddle point) on this path is characterized by maximum electron density, known as the (3, −1) bond critical point (BCP) where $\nabla\rho(r) = 0$. A range of properties, such as electron density $\rho(r)$, Laplacian $\nabla^2\rho(r)$, total density $H(r)$, local electron potential $V(r)$, Lagrangian kinetic electron density (g), and eigenvalues of the Hessian matrix (λ_1, λ_2, and λ_3), can be investigated from this point.

Within the framework of QTAIM, intermolecular interactions can be assessed based on the $\nabla^2\rho$ parameter and H_{BCP} parameter, leading to their categorization into three distinct types: weak covalent bonds (noncovalent interactions) are identified when $\nabla^2\rho$ has a positive value (+) and H_{BCP} is positive (+); moderate (partial) covalent bonds occur when $\nabla^2\rho$ is positive (+) and H_{BCP} is negative (−); and strong

https://doi.org/10.1021/acsomega.4c00759
ACS Omega 2024, 9, 16701−16715

Table 3. Second-Order Perturbation Theory Analysis of the Fock Matrix

complex		donor (i)	acceptor (j)	$E^{(2)}$ (kcal/mol)	$E(j) - E(i)$ (a.u.)	$F(i,j)$ (a.u)
Cur−ACE2	unit 1 to 7	BD(2) C17−C21	BD*(1) C182−H187	0.330	0.810	0.015
	unit 3 to 7	BD(1) C69−H70	BD*(2) C182−C183	0.160	0.550	0.008
	unit 5 to 7	BD(1) C102−H103	BD*(1) C174−H191	0.120	1.060	0.010
	unit 6 to 7	LP(3) O152	BD*(1) C205−H206	0.310	0.690	0.013
	unit 7 to 1	BD(1) C182−H187	BD*(2) C17−C21	0.490	0.540	0.015
	unit 7 to 2	LP(1) O200	BD*(1) C39−H40	0.160	0.870	0.011
	unit 7 to 3	BD(1) C183−H188	BD*(1) C69−H70	0.560	0.910	0.020
	unit 7 to 6	LP(1) O204	BD*(1) C149−H150	0.660	0.740	0.020
CD1−ACE2	unit 1 to 6	BD(1) C29−H30	BD*(2) C169−C170	0.710	0.530	0.017
	unit 2 to 6	BD(1) C46−H47	LV(1) C168	0.210	0.340	0.008
	unit 3 to 6	BD(2) C59−O60	LV(1) C155	0.850	0.310	0.014
	unit 4 to 6	LP(1) O 92	BD*(1) C171−C188	0.120	1.140	0.010
	unit 5 to 6	BD(1) N131−H133	BD*(2) C172−O201	0.200	0.670	0.010
	unit 6 to 1	BD(1) C178−H199	BD*(1) C19−H20	0.460	0.870	0.018
	unit 6 to 2	LP(1) C146	BD*(1) C46−H47	1.450	0.520	0.024
	unit 6 to 3	BD(2) C153−C165	BD*(1) N73−H75	1.570	0.550	0.026
	unit 6 to 5	BD(2) C172−O201	BD*(1) C127−N131	0.420	0.830	0.017
CD2−ACE2	unit 1 to 6	BD(1) C29−H30	BD*(2) C180−C181	0.610	0.530	0.016
	unit 2 to 6	BD(1) C46−H47	BD*(2) C158−C159	0.120	0.490	0.007
	unit 3 to 6	LP(1) O 72	BD*(2) C166−C167	0.280	0.570	0.011
	unit 5 to 6	LP(1) N143	LV (1) C184	0.100	0.190	0.004
	unit 6 to 1	BD(1) C181−H207	BD*(1) C19−H20	0.490	0.870	0.018
	unit 6 to 2	BD(2) C158−C159	BD*(1) C46−H47	1.720	0.640	0.030
	unit 6 to 3	BD(2) C177−C178	BD*(1) N85−H87	2.300	0.590	0.033
	unit 6 to 5	LP (3) O210	BD*(1) C139−N143	0.520	0.680	0.017
CD3−ACE2	unit 1 to 6	BD(1) C19−H20	BD*(1) C175−H203	0.820	1.060	0.026
	unit 2 to 6	BD(1) C46−H47	BD*(2) C169−C170	0.620	0.490	0.016
	unit 3 to 6	LP(1) O72	BD*(2) C154−C155	0.300	0.580	0.012
	unit 4 to 6	LP(1) O104	BD*(1) C171−C198	0.120	1.110	0.010
	unit 5 to 6	LP(1) N143	LV(1) C171	0.170	0.190	0.005
	unit 6 to 1	BD(1) C175−H203	BD*(1) C19−H20	0.830	0.870	0.024
	unit 6 to 2	BD(2) C169−C170	BD*(1) C46−H47	0.370	0.640	0.014
	unit 6 to 3	BD(2) C178−C179	BD*(1) N85−H87	2.110	0.590	0.031
	unit 6 to 5	BD(2) N172−C173	BD*(1) N143−H145	0.370	0.690	0.014
CD4−ACE2	unit 1 to 6	BD(1) C29−H30	BD*(2) C183−C184	0.660	0.530	0.017
	unit 3 to 6	BD(2) C59−O60	BD*(2) C145−C173	0.300	0.440	0.010
	unit 6 to 1	BD(2) C183−C184	BD*(1) C29−H30	0.540	0.670	0.017
	unit 6 to 2	BD(2) C156−C157	BD*(1) C46−H47	0.460	0.650	0.016
	unit 6 to 3	BD(2) C152−C164	BD*(1) N73−H75	2.670	0.550	0.034
	unit 6 to 5	BD(2) C175−O202	BD*(1) C127−N131	0.150	0.820	0.010

covalent bonds emerge when $\nabla^2\rho$ is negative (−) and H_{BCP} is negative (−).

As shown in Table 4, the interaction between curcumin and the active pocket of ACE2 is formed from 18 bonds. From these data, it can be seen that all of the interactions are classified as weak covalent interactions, as indicated by all positive $\nabla^2\rho$ and positive H_{BCP} values. This interaction is also observed when the CD1 ligand interacts with the active pocket of ACE2. All 14 interactions show positive $\nabla^2\rho$ and H_{BCP} values, so all interactions are classified as weakly covalent. Different phenomena occur in the complex system between ACE2 and CD2, CD3, and CD4. Nine weak covalent interactions were formed. In addition, a strong covalent interaction is also formed, as can be seen from the values of X and Y, which are both negative. This classification of strong covalent interactions was also found for the CD3-ACE2 and CD4-ACE2 complexes.

These results were supported by the $|V|/G$ ratio of each system. Based on the literature, this ratio divides the strength of the interaction into three types. When $|V|/G > 2$, the degree of H_{BCP}/ρ_{BCP} bonding is large and negative because the potential energy is greater than that in the average virial regime; therefore, its absolute value provides a measure of covalent character. In this study, this value indicates a strong interaction between the ligand compound and ACE2. On the other hand, when $1 < |V|/G < 2$, the degree of H_{BCP}/ρ_{BCP} bonding is small and negative, owing to the dominance of potential energy over H_{BCP}. This indicates a moderate interaction. For the third type of interaction, when $|V|/G < 1$, the kinetic energy becomes the main contributor and the degree of bonding becomes positive. This ratio leads to weak interactions. From the same data in Table 4, the $|V|/G$ ratio of all interactions in the curcumin-ACE2 and CD1-ACE2 complexes was below 1, so all interactions were classified as weak, as the results of the previous analysis. Meanwhile, in the CD2-ACE2, CD3-ACE2, and CD4-ACE2 complexes, there was one interaction with $|V|/G$ ratios above 2, i.e., 4.365, 4.291, and 4.476, respectively, so it was classified as strong covalent.

https://doi.org/10.1021/acsomega.4c00759
ACS Omega 2024, 9, 16701−16715

Table 4. QTAIM Analysis of All Systems

system	BCP	interaction	ρ	$\nabla^2\rho$	H_{BCP}	V_{BCP}	G_{BCP}	λ_1	λ_2	λ_3	$\|V\|/G$
Cur−ACE2	255	103(H)−191(H)	0.005	0.014	0.001	−0.002	0.003	−0.002	0.018	−0.001	0.807
	263	124(O)−191(H)	0.003	0.009	0.000	−0.001	0.002	0.001	0.000	0.008	0.730
	269	124(O)−197(O)	0.005	0.021	0.001	−0.003	0.004	−0.001	0.009	0.013	0.687
	274	40(H)−200(O)	0.006	0.022	0.001	−0.003	0.004	0.003	0.003	0.016	0.740
	292	46(O)−200(O)	0.008	0.034	0.002	−0.005	0.007	−0.006	−0.006	0.047	0.741
	312	173(H)−22(H)	0.005	0.016	0.001	−0.002	0.003	−0.001	0.014	0.003	0.762
	335	22(H)−196(O)	0.003	0.011	0.001	−0.001	0.002	0.013	−0.001	−0.001	0.639
	337	211(H)−18(H)	0.007	0.022	0.001	−0.004	0.005	0.004	0.013	0.005	0.792
	352	209(H)−61(C)	0.000	0.001	0.000	0.000	0.000	0.000	0.001	0.000	0.556
	371	17(C)−187(H)	0.010	0.032	0.001	−0.005	0.007	0.005	0.026	0.001	0.799
	408	146(H)−182(C)	0.003	0.009	0.001	−0.001	0.002	0.000	0.000	0.010	0.645
	432	70(H)−188(H)	0.010	0.029	0.001	−0.005	0.006	0.023	−0.008	0.014	0.801
	450	142(H)−184(C)	0.008	0.023	0.001	−0.004	0.005	−0.003	−0.004	0.030	0.818
	477	203(H)−94(H)	0.002	0.005	0.000	−0.001	0.001	0.006	0.000	−0.001	0.702
	485	204(O)−150(H)	0.009	0.032	0.002	−0.005	0.007	0.001	0.012	0.019	0.751
	491	202(O)−164(H)	0.003	0.011	0.001	−0.001	0.003	0.002	0.005	0.004	0.482
	493	204(O)−164(H)	0.006	0.022	0.001	−0.003	0.004	0.001	0.018	0.004	0.752
	509	206(H)−152(O)	0.006	0.021	0.001	−0.003	0.004	0.013	0.001	0.007	0.754
CD1−ACE2	244	60(O)−155(C)	0.009	0.036	0.002	−0.006	0.007	0.005	0.002	0.029	0.775
	267	63(H)−135(C)	0.006	0.018	0.001	−0.003	0.004	0.001	0.002	0.015	0.786
	307	58(H)−140(C)	0.007	0.021	0.001	−0.004	0.005	0.000	−0.001	0.023	0.811
	323	65(H)− 138(C)	0.006	0.018	0.001	−0.003	0.004	−0.002	0.002	0.017	0.798
	332	71(H)−149(C)	0.006	0.019	0.001	−0.003	0.004	−0.003	0.001	0.021	0.793
	378	203(H)−92(O)	0.004	0.018	0.001	−0.002	0.003	0.000	−0.001	0.019	0.686
	400	92(O)−202(H)	0.004	0.018	0.001	−0.002	0.003	0.005	0.000	0.013	0.670
	418	51(O)−173(C)	0.005	0.000	0.001	−0.002	0.003	0.001	0.001	0.015	0.714
	420	45(H)−169(C)	0.003	0.011	0.001	−0.001	0.002	0.000	−0.001	0.011	0.682
	448	131(N)−201(O)	0.010	0.049	0.003	−0.007	0.010	−0.004	0.004	0.049	0.746
	456	198(H)−30(H)	0.013	0.043	0.002	−0.008	0.009	−0.006	0.030	0.019	0.823
	467	198(H)−20(H)	0.012	0.043	0.002	−0.007	0.009	−0.013	0.019	0.037	0.803
	483	199(H)−20(H)	0.012	0.038	0.002	−0.007	0.008	0.051	−0.006	−0.007	0.813
	487	199(H)−29(C)	0.007	0.022	0.001	−0.004	0.005	0.002	0.008	0.012	0.813
CD2−ACE2	247	93(H)−216(C)	0.005	0.015	0.001	−0.002	0.003	0.001	−0.001	0.016	0.776
	254	72(O)−167(C)	0.009	0.036	0.002	−0.006	0.007	0.005	0.002	0.029	0.773
	302	177(C)−87(H)	0.012	0.034	0.001	−0.006	0.007	−0.008	−0.004	0.047	0.789
	318	70(H)−152(C)	0.007	0.021	0.001	−0.004	0.004	0.000	−0.001	0.022	0.810
	335	77(H)−150(C)	0.006	0.018	0.001	−0.003	0.004	−0.001	0.003	0.016	0.802
	390	192(C)−59(H)	0.001	0.002	0.000	0.000	0.000	0.000	0.000	0.002	0.553
	399	159(C)−158(C)	0.309	−0.903	−0.321	−0.417	0.095	−0.363	−0.175	−0.365	4.365
	406	197(C)−104(O)	0.004	0.016	0.001	−0.002	0.003	0.001	−0.001	0.016	0.675
	425	104(O)−211(H)	0.004	0.018	0.001	−0.002	0.003	0.004	0.000	0.013	0.668
	449	45(H)−181(C)	0.003	0.011	0.001	−0.001	0.002	0.533	0.000	0.011	0.694
CD3−ACE2	245	93(H)−199(C)	0.003	0.016	0.001	−0.002	0.003	0.000	−0.001	0.015	0.770
	251	72(O)−155(C)	0.009	0.036	0.002	−0.006	0.007	0.005	0.002	0.029	0.772
	272	75(H)−151(C)	0.006	0.018	0.001	−0.003	0.004	0.002	0.002	0.014	0.782
	298	179(C)−87(H)	0.011	0.033	0.001	−0.005	0.007	−0.007	−0.004	0.044	0.784
	314	70(H)−152(C)	0.008	0.022	0.001	−0.004	0.005	0.000	−0.001	0.023	0.814
	331	77(H)−148(C)	0.006	−0.001	0.001	−0.003	0.004	−0.001	0.003	0.016	0.797
	345	166(C)−186(C)	0.317	−0.937	−0.337	−0.439	0.102	0.231	−0.644	−0.524	4.290
	385	59(H)−194(C)	0.001	0.002	0.000	0.000	0.000	0.001	0.000	0.002	0.556
	424	104(O)−217(H)	0.005	0.021	0.001	−0.003	0.004	0.005	0.000	0.016	0.689
	441	51(O)−173(C)	0.005	0.016	0.001	−0.002	0.003	0.002	0.001	0.014	0.706
	454	172(N)−145(H)	0.009	0.035	0.002	−0.005	0.007	−0.005	−0.005	0.045	0.755
	462	204(H)−22(O)	0.003	0.010	0.001	−0.001	0.002	−0.002	0.000	0.011	0.679
CD4−ACE2	235	81(H)−173(C)	0.006	0.016	0.001	−0.003	0.003	−0.002	0.001	0.018	0.794
	236	146(C)−60(O)	0.009	0.034	0.002	−0.005	0.007	0.004	−0.003	0.033	0.766
	262	148(C)−69(H)	0.006	0.020	0.001	−0.003	0.004	0.000	−0.004	0.023	0.795
	298	75(H)−164(C)	0.012	0.034	0.001	−0.005	0.007	−0.001	0.001	0.033	0.790
	301	139(C)−58(H)	0.007	0.020	0.001	−0.003	0.004	−0.003	0.000	0.024	0.795
	328	151(C)−71(H)	0.006	0.018	0.001	−0.003	0.004	0.000	0.002	0.016	0.783
	357	158(C)−162(C)	0.307	−0.899	−0.316	−0.406	0.091	0.120	−0.444	−0.575	4.476

https://doi.org/10.1021/acsomega.4c00759
ACS Omega 2024, 9, 16701−16715

Table 4. continued

system	BCP	interaction	ρ	$\nabla^2\rho$	H_{BCP}	V_{BCP}	G_{BCP}	λ_1	λ_2	λ_3	$\lvert V\rvert/G$
	378	201(H)−92(O)	0.005	0.021	0.001	−0.003	0.004	−0.002	−0.002	0.025	0.718
	407	92(O)−202(O)	0.003	0.013	0.001	−0.002	0.002	0.004	0.002	0.007	0.648
	432	202(O)−131(N)	0.010	0.044	0.002	−0.007	0.009	0.003	−0.007	0.049	0.741
	446	188(H)−22(O)	0.006	0.020	0.001	−0.003	0.004	0.007	−0.002	0.015	0.748
	449	188(H)−30(H)	0.012	0.040	0.002	−0.007	0.008	0.003	0.024	0.012	0.810
	468	203(H)−29(C)	0.005	0.015	0.001	−0.002	0.003	0.000	0.010	0.006	0.748

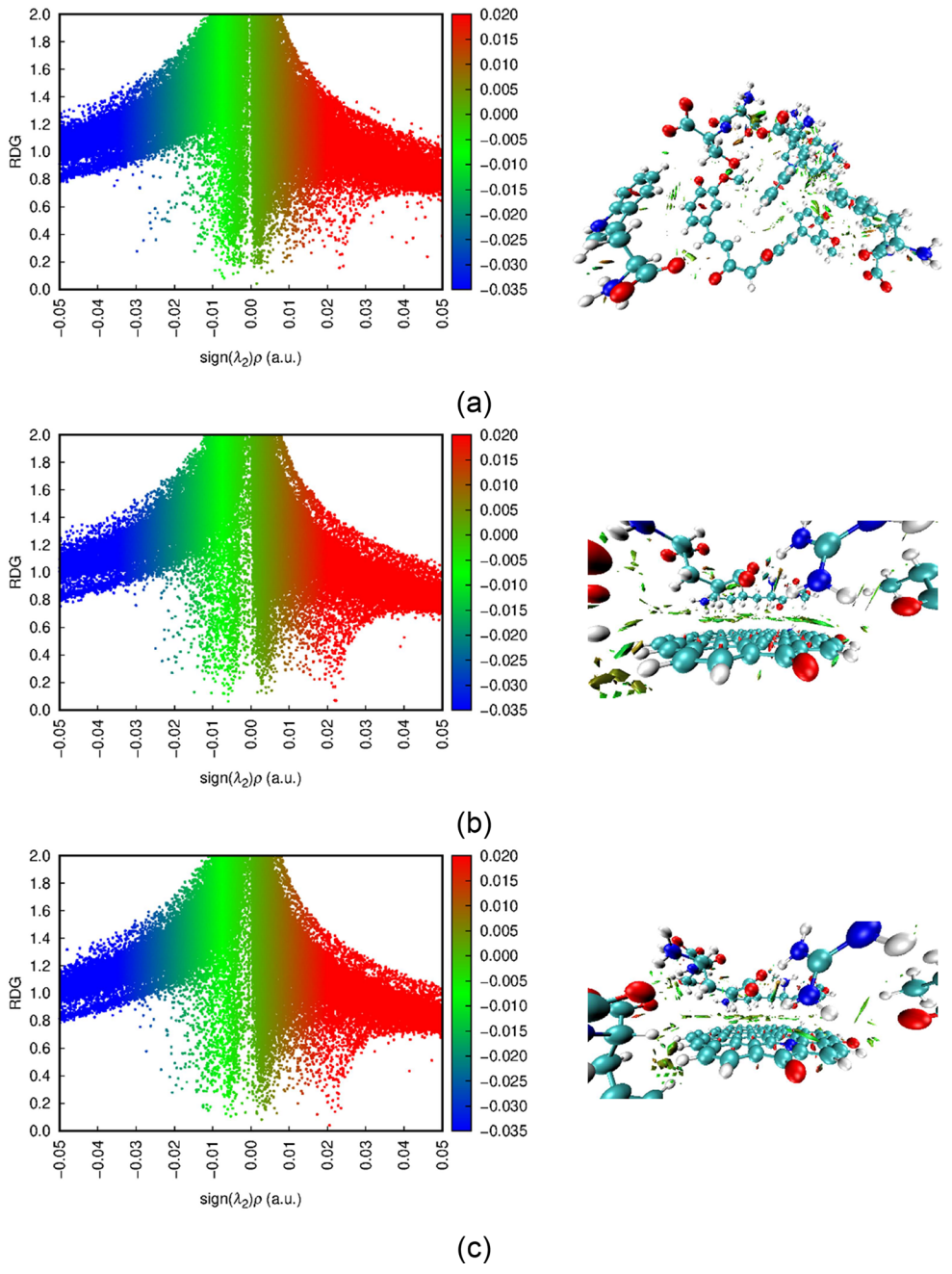

Figure 2. RDG (Y Axis) vs Sign $(\lambda_2)\rho$ (X axis) and NCI of (a) Cur-ACE2, (b) CD1-ACE2, and (c) CD2-ACE2.

3.4. NCI-RDG Analysis. Figures 2 and 3 provide visual representations of the correlation between the reduced density gradient (RDG) and the sign of $(\lambda_2)\rho$ as well as the noncovalent NCI interaction iso-surfaces for each ligand-ACE2 system. RDG is a valuable tool for gaining insights into the nature and intensity of interactions and distinguishing between attractive and repulsive forces. Specifically, a more negative $(\lambda_2)\rho$ value (with a charge density of −0.04) signifies a stronger attractive force, encompassing phenomena like hydrogen bonds and dipole−dipole interactions. Conversely, a progressively positive $(\lambda_2)\rho$ value, corresponding to a charge density (ρ) of 0.04, suggests a robust repulsive interaction or

https://doi.org/10.1021/acsomega.4c00759
ACS Omega 2024, 9, 16701−16715

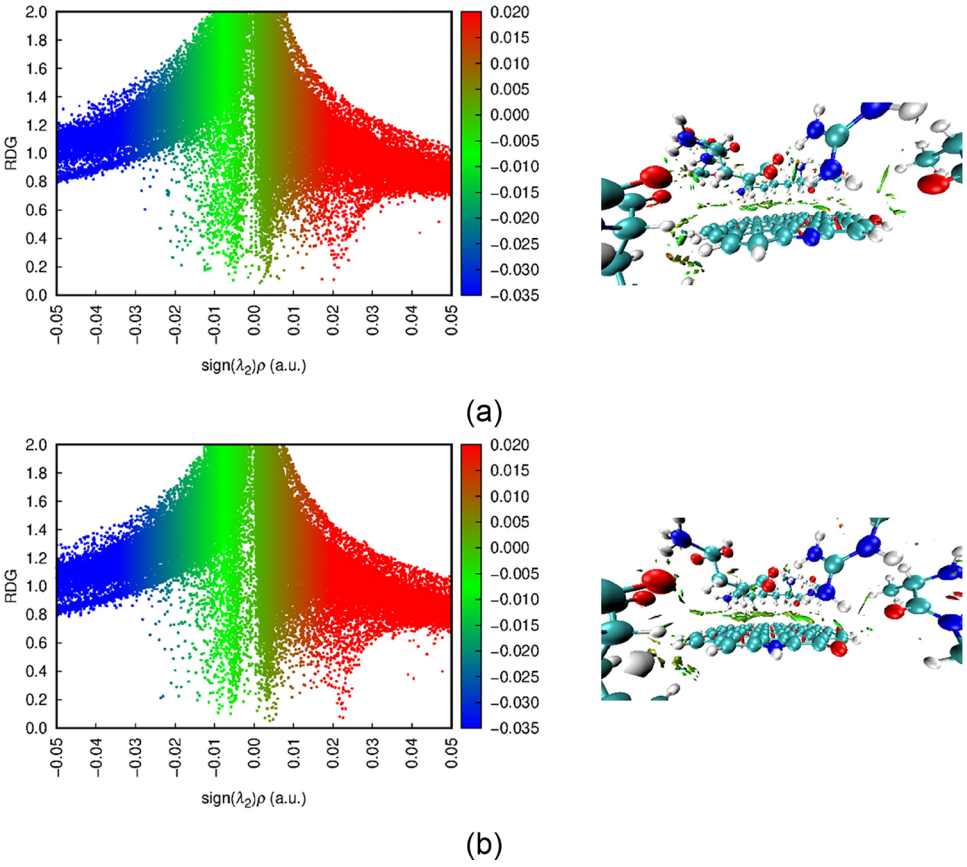

Figure 3. RDG (Y axis) vs Sign $(\lambda_2)\rho$ (X axis) and NCI of (a) CD3-ACE2 and (b) CD4-ACE2.

pronounced nonbonded overlap. Additionally, when the charge density (ρ) approaches zero, it signifies the presence of van der Waals (vdW) forces.

As shown in Figure 2 and 3, the 3D iso-surfaces of all the systems showed the presence of green patches between the surface of the ligand and the active pocket of ACE2. This result can also be observed in the 2D-RDG graph. The projection of green patches appeared between 0 and −0.01 a.u., which confirmed that a weak dispersive force was dominant in stabilizing the complex formation between the ligand and ACE2. A higher density of green spikes was observed in the CD1, CD2, CD3, and CD4-ACE2 complexes than that in the curcumin-ACE2 complex. On the other hand, the 3D isosurface also showed the presence of red patches on the benzene ring of curcumin and other graphene-based ligands. This result is consistent with the appearance of a red peak in the 0.2 au region in the 2D-RDG graph, which is associated with steric repulsion. In addition, in the 2D-RDG graph, blue dots appear between −0.02 and −0.03 au. If confirmed from the 3D isosurface, it is known that the appearance of these blue dots is due to intramolecular hydrogen bonding in the active pocket of ACE2.

3.5. Molecular Docking. In this study, curcumin was used as a positive control because it has antiviral activity against viruses, such as HIV, herpes simplex virus, influenza, and hepatitis B and C. In addition, the use of curcumin as an ACE2 inhibitor has also been investigated by previous researchers, considering the type of binding involved, such as conventional hydrogen bonds, carbon−hydrogen bonds, and $\pi-\sigma$ interactions. YASARA docking studies of the four ligand molecules and ACE2 yielded information about the binding energy value.

More positive binding energy values indicate a higher affinity of the ligand to the ACE2 receptor, as measured by YASARA. The stability of the interaction between these ligands and ACE2 was measured by the binding energy, which increases as the value moves toward a positive value. Furthermore, the stronger the interaction between the ligand and receptor, the higher the binding energy value. Table 5 shows the results of the interaction of ACE2 with the four different ligand molecules.

From Table 5, curcumin, as a comparison ligand, had the lowest affinity value of −7.681 kcal/mol. This indicates that curcumin and ACE2 have weaker and less stable bonds in comparison to the other ligands. Meanwhile, the high binding energy value of −10.677 kcal/mol for the CD3 ligand suggests that this ligand forms a strong and stable bond, suggesting that

Table 5. Binding Energy Data of the Ligand to the ACE2

ligand	binding energy (kcal/mol)	contacting receptor residues
curcumin	−7.681	A PHE 40 A SER 43 A SER 44 A SER 47 A MET 62 A TRP 69 A LEU 73 A ALA 99 A ALA 348 A TRP 349 A ASP 350 A ASP 382 A TYR 385 A PHE 390 A LEU 391 A ARG 393 A ASN 394 A LYS 562
CD1	−10.648	A ASN 33 A HIS 34 A GLU 37 A LYS 353 A GLY 354 A ALA 386 A ALA 387 A ARG 393
CD2	−10.567	A ASN 33 A HIS 34 A GLU 37 A ASP 38 A LYS 353 A GLY 354 A ALA 386 A ALA 387 A ARG 393
CD3	−10.677	A ASN 33 A HIS 34 A GLU 37 A ASP 38 A LYS 353 A GLY 354 A ALA 386 A ALA 387 A ARG 393
CD4	−10.529	A ASN 33 A HIS 34 A GLU 37 A LYS 353 A GLY 354 A ALA 386 A ALA 387 A ARG 393

https://doi.org/10.1021/acsomega.4c00759
ACS Omega 2024, 9, 16701−16715

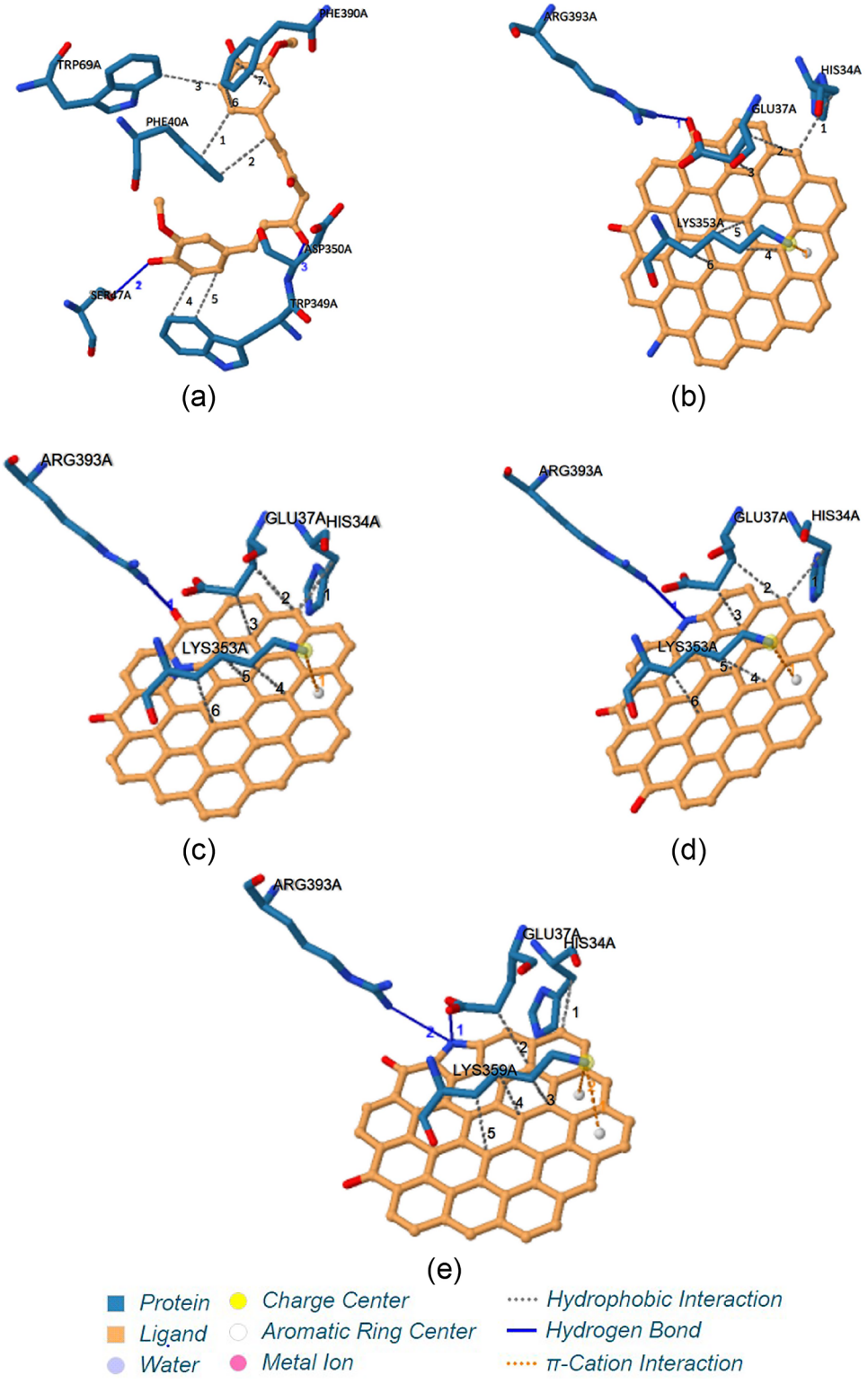

Figure 4. Interaction of ACE2 amino acid residue with (a) CUR, (b) CD1, (c) CD2, (d) CD3, and (e) CD4 from molecular docking result.

it has an excellent potential to create a bond with ACE2 and block the binding of SARS-CoV-2 into human cells. However, it is possible that other ligand compounds have potential as anti-COVID-19 agents because their affinity values do not differ significantly from those of the CD3 ligand. Other data acquired from the molecular docking procedure, such as the binding site, type of bond, distance, and ACE2 amino acid residues implicated in bonding with the ligand chemical, can be analyzed to further investigate the potential of ligand compounds as anti-COVID-19 drugs.

Alazmi et al. analyzed natural compounds as ACE2 inhibitors, with the highest binding energy values being andrographolide (−9.100 kcal/mol) and pterostilbene (−8.900 kcal/mol).[1] Khelfaoui et al. analyzed various commercial drugs as ACE2 inhibitors. Of the eight drugs analyzed, the best 3 materials were obtained, namely Delapril

https://doi.org/10.1021/acsomega.4c00759
ACS Omega 2024, 9, 16701−16715

(−6.981 kcal/mol) and Lisinopril (−6.689 kcal/mol), with RMSDs 2.257 and 1.541 Å, respectively.[2] Meanwhile, Srivastava found that cinnamic acid (−5.200 kcal/mol), thymoquinone (−4.710 kcal/mol), and andrographolide (Kalmegh) (−4.000 kcal/mol) against ACE2.[3] From these studies, it can be seen that CD1, CD2, CD3, and CD4 are still superior compounds against ACE2.

The most important interactions, or those observed from the smallest interatomic distance, were analyzed by using the PLIP software for further identification. These results show that curcumin compounds can interact with residues via hydrophobic interactions with PHE 40, TRP 69, TRP 349, and PHE 390, as depicted in Figure 4.

In addition to hydrophobic interactions, these compounds are capable of forming hydrogen bonds with SER 47 and ASP 350. The CD1 ligand compound was able to form hydrophobic interactions with HIS 34, GLU 37, and LYS 353 residues. In addition, hydrogen bonds with ARG 393 and π−cation interactions with LYS 353 were also formed. The CD2 ligand was able to form hydrophobic interactions with three different residues: HIS 34, GLU 37, and LYS 353. In addition, hydrogen bonds were formed with ARG 393, and π−cation interactions with LYS 353 were formed. Most importantly, the CD3 ligand molecule was able to create hydrophobic contacts with HIS 34, GLU 37, and LYS 353, making it the highest-affinity ligand. Similar to another ligand, this ligand is also capable of forming hydrogen bonds with ARG 393 and π−cation interactions with LYS 353. The last ligand compound, CD4, can form hydrophobic bonds with residues HIS 34, GLU 37, and LYS 353. It is also capable of forming hydrogen bonds with GLU 37 and ARG 393 and forms two π-cation interactions with LYS 353. Based on these findings, it appears that residues HIS 34, GLU 37, LYS 353, and ARG 393 are the primary contact points between the ligands and ACE2. These residues are located on the active site of ACE2, which consists of SER 19, GLN 24, THR 27, PRO 28, ASP 30, LYS 31, PHE 32, TYR 41, GLN 42, LEU 45, MET 82, TYR 83, ASN 330, LEU 351, GLY 352, LYS 353, GLY 354, ASP 355, ARG 357, ALA 386, and ARG 393. This suggests that the four sample ligands have the potential to reduce the activity of ACE2, thereby blocking the binding of the RBD of the SARS-CoV-2 virus and preventing human exposure to this pathogen.

3.6. Molecular Dynamics Simulation Results. To obtain more understanding of the protein and docked complexes in biological conditions, a molecular dynamics (MD) simulation was run on all system complexes. The different ligand interaction types as a function of the simulation time are displayed in Figure 5. Every molecule of protein or nucleic acid has a single layout. Three different kinds of contacts are displayed: ionic interactions (blue), hydrogen bonds (red), and hydrophobic contacts (green). If a particular residue makes many types of interaction with the ligand, combinations of these three colors may also be visible. According to a recent study, the main prevailing mechanisms behind the increased binding of SARS-CoV-2 include the hydrogen bonding network and hydrophobic interactions. This study also demonstrated. Hydrogen bonding dominated the interaction between ACE2 with nanocarbon material and curcumin. Overall curcumin and nanomaterial carbon form bonds in the form of hydrogen bonds, on average occurring at residue numbers 37, 38, 324, 325, 353, 354, 356, 383, 386, 387, and 393. While generally hydrophobic bonds occur at residue numbers 324 and 325.

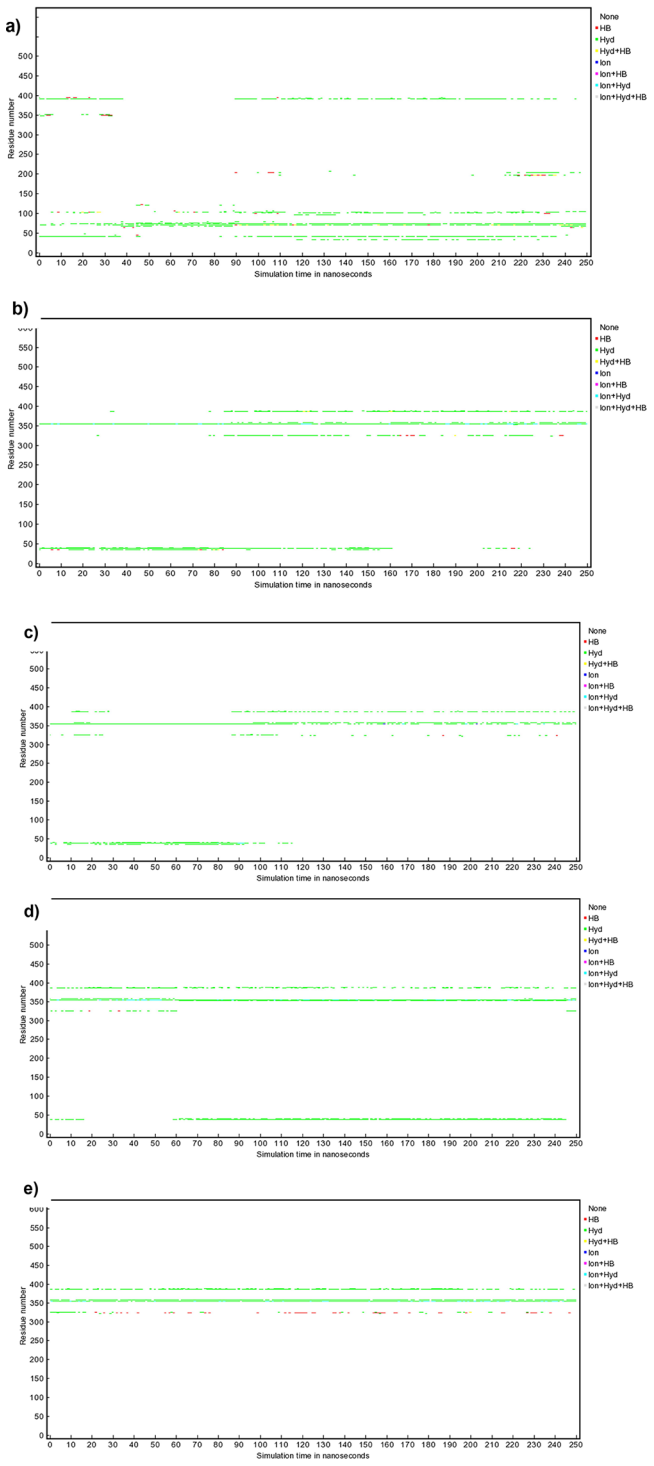

Figure 5. Per-residue contact with ligand at (a) cur-ACE2, (b) CD1-ACE2, (c) CD2-ACE2, (d) CD3-ACE2, and (e) CD4-ACE2 complexes.

3.6.1. RMSD. The plot in Figure 6 shows the RMSD of the Cα atoms of all of the ligand-ACE2 complexes. In the case of the curcumin-ACE2 complex, the average value was 1.863 Å, with fluctuations at approximately 10.6, 68, 148, 209, 552, 215, and 241 ns, indicating a loss of stability in these regions. In the case of CD3-ACE2 and CD4-ACE2 complexes, the RMSD values were slightly increase of average value than curcumin, which is 1.987 Å. Minor fluctuations only occurred at some points in both complexes. However, the CD1-ACE2 and CD2-

https://doi.org/10.1021/acsomega.4c00759
ACS Omega 2024, 9, 16701−16715

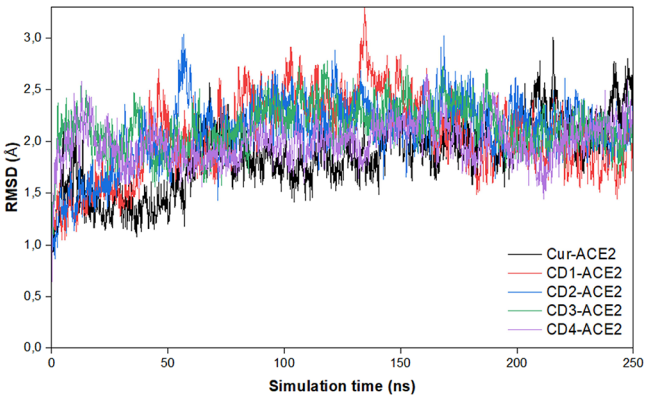

Figure 6. Representation of RMSD over a time of 250 ns of all complexes.

ACE2 complexes averaged higher RMSD values and larger fluctuations. Especially for CD1-ACE2, a considerable increase in RMSD value occurred at 46−134 ns, then dropped regularly to 185 ns.

The average values of RMSD for cur-ACE2, CD1-ACE2, CD2-ACE2, CD3-ACE2, and CD4-ACE2 are 1.863, 2.061, 2.098, 2.042, and 1.987, respectively. Based on the literature, a smaller RMSD value indicates higher stability of the complex. These results suggest that curcumin is the most stable agent for forming complexes with ACE2. In contrast to curcumin and other samples, CD3 and CD4 exhibit insignificant fluctuations. Thus, it can be concluded that the CD3-ACE2 and CD4-ACE4 complexes are stable, as well.

3.6.2. RMSF. The RMSF value is a dynamic parameter that measures the residual flexibility in the side chains of a protein. The plot in Figure 7 shows the RMSF of all ligand-ACE2 complexes. The average RMSF of the overall positions of Cur-ACE2, CD1-ACE2, CD2-ACE2, CD3-ACE2, and CD4-ACE2 were 1.235, 1.429, 1.327, 1.241, and 1.291 Å, respectively. The total fluctuation of all systems was approximately the same except for a few residual fluctuations, such as residue 158 in the CD2-ACE2 complex and residue 291−309 in the CD1-ACE2 complex.

3.6.3. Radius of Gyration (R_g). The radius of gyration (R_g) is used to describe the compactness of the protein structure. This parameter is defined as the mass-weighted root mean square distance for the collection of atoms from the center of mass. The simulation demonstrates that a system is more rigid and compact when the degree of fluctuation is lower and remains consistent. The plot in Figure 8 shows the R_g values of all ligand-ACE2 complexes. In terms of the consistency of

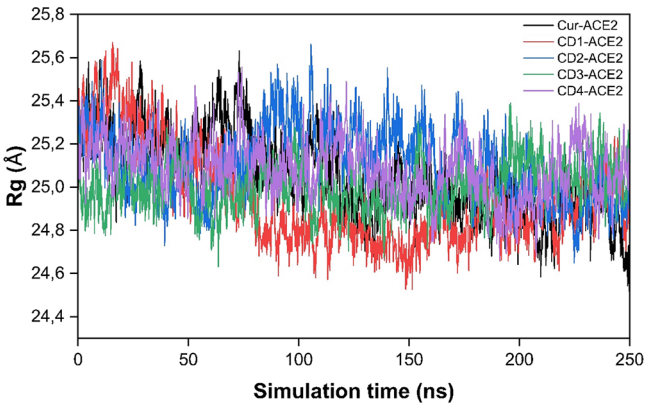

Figure 8. Representation of radius of gyration (R_g) over a time of 250 ns of all complexes.

variations over the course of the simulation, the R_g of the CD3-ACE2 and CD4-ACE2 complexes is found to be nearly steady. In the meantime, the cur-ACE2 and CD1-ACE2 complexes experience a drop in R_g. In CD2-ACE2, it fell between 0 and 55 ns, then rose between 55 and 92 ns, and then fell between 92 and 250 ns once again. R_g changes could be the consequence of specific conformational changes or protein folding.

The R_g values for cur-ACE2, CD1-ACE2, CD2-ACE2, and CD4-ACE2 are 25.05, 25.146, 25.206, and 25.084 Å, respectively. The average R_g value for the CD3-ACE2 complex is the lowest, at 25.00 Å. Therefore, CD3 > curcumin > CD4 > CD1 > CD2 should be the order of compactness and rigidity.

3.6.4. Solvent Accessible Surface Area. The solvent accessible surface area (SASA) was determined to investigate the solvent accessibility of all ligand-ACE2 complexes. Greater SASA values suggest that the protein volume is expanding, and little fluctuation is anticipated during the simulation period. Any tiny molecule binding may cause SASA to change and sometimes has a significant impact on the structure of the protein. The results of SASA and MolSA for all complexes are shown in Figure 9. When curcumin is compared to graphene (CD), its SASA value is found to be lower in the majority of the frames. This suggests that the curcumin binding may inhibit the expansion of proteins. While the CD1-ACE2

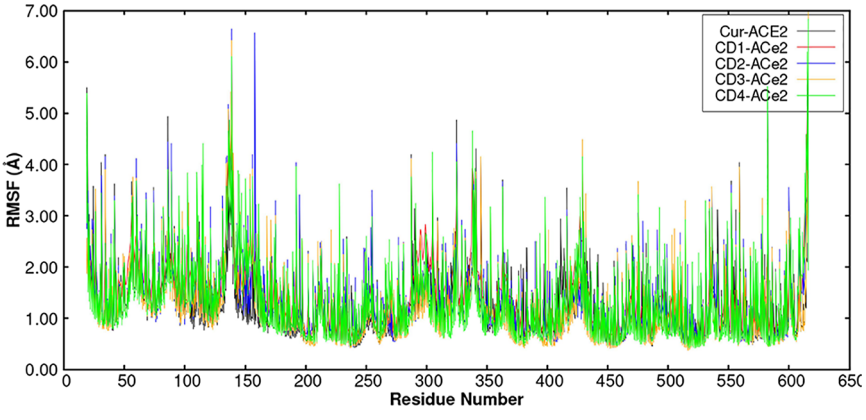

Figure 7. Representation of RMSF over 250 ns of all complexes.

https://doi.org/10.1021/acsomega.4c00759
ACS Omega 2024, 9, 16701−16715

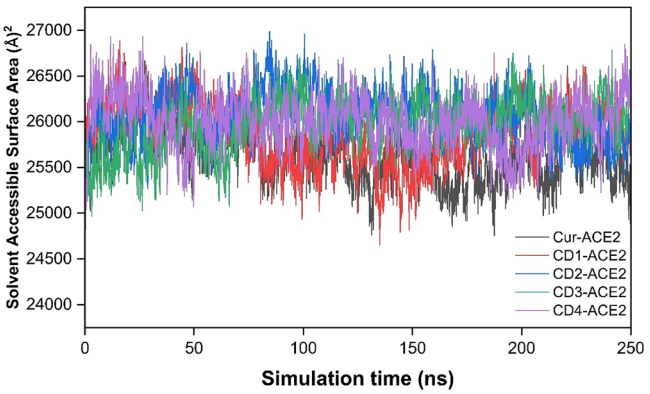

Figure 9. Representation of SASA over the time of 250 ns for all complexes.

complex achieved nearly the same SASA value as curcumin between 0 and 144 ns, there was an increase in SASA value fluctuation beyond that point.

Furthermore, compared to other complexes, the CD4-ACE2 complex exhibits normal fluctuations. Whereas in the CD2-ACE2 complex, the highest fluctuation occurs (56−115 ns), so that this reveals a conformational state with higher protein expansion. While the small protein expansion that occurs in CD3-ACE2 is characterized by the rise and fall of SASA values from 0 to 73 ns.

This high SASA value indicated the migration of ligand to the solvent side, where the active pocket of ACE2 became highly solvated and minimally compacted.[56,57] The average SASA values for all complexes are 25631.84, 25995.73, 26074.905, 25973.79, and 25993.12 Å^2 for cur-ACE2, CD1-ACE2, CD2-ACE2, CD3-ACE2, and CD4-ACE2, respectively. So based on these values, the order of compatibility of the simulated complex is cur-ACE2 > CD3-ACE2 > CD4-ACE2 > CD1-ACE2, and CD2-ACE3.

4. CONCLUSIONS

In this study, four carbon dot compounds in the form of amino, graphitic, pyridinic, and pyrrolic groups were theoretically analyzed by DFT calculations, molecular docking calculations, and molecular dynamics simulations. Based on the binding affinity results, these four compounds have a higher value when compared to the value of the control ligand, curcumin; therefore, they are very promising as inhibitors against SARS-CoV-2. This is consistent with the results of the DFT calculations. The data for HOMO−LUMO, NBO, QTAIM, and NCI-RDG also indicated that the interaction ability of these four compounds was better than that of the control ligand. Moreover, the MD simulation data show that these compounds have a relatively good stability profile, especially for pyridinic compounds. These findings may contribute to the further development of inhibitors against SARS-CoV-2.

AUTHOR INFORMATION

Corresponding Authors

Atthar Luqman Ivansyah − *Master Program in Computational Science, Faculty of Mathematics and Natural Sciences and Department of Physics, Institut Teknologi Bandung, Bandung, West Java 40132, Indonesia;* orcid.org/0000-0001-9716-8982; Email: atthar@csx.itb.ac.id

Fahdzi Muttaqien − *Master Program in Computational Science, Faculty of Mathematics and Natural Sciences and Department of Physics, Institut Teknologi Bandung, Bandung, West Java 40132, Indonesia;* orcid.org/0000-0001-8970-444X; Email: fahdzi@itb.ac.id

Ferry Iskandar − *Research Center for Nanosciences and Nanotechnology and Department of Physics, Institut Teknologi Bandung, Bandung, West Java 40132, Indonesia; Collaboration Research Center for Advanced Energy Materials, National Research and Innovation Agency - Institut Teknologi Bandung, Bandung 40132, Indonesia;* orcid.org/0000-0002-0464-0035; Email: ferry@fi.itb.ac.id

Authors

Harsiwi Candra Sari − *Master Program in Computational Science, Faculty of Mathematics and Natural Sciences, Institut Teknologi Bandung, Bandung, West Java 40132, Indonesia*

Haliza Hasnia Putri − *Master Program in Computational Science, Faculty of Mathematics and Natural Sciences, Institut Teknologi Bandung, Bandung, West Java 40132, Indonesia*

Pinantun Wiguna Kusuma Paksi − *Master Program in Computational Science, Faculty of Mathematics and Natural Sciences, Institut Teknologi Bandung, Bandung, West Java 40132, Indonesia*

Gabriel Hidayat − *Master Program in Computational Science, Faculty of Mathematics and Natural Sciences, Institut Teknologi Bandung, Bandung, West Java 40132, Indonesia*

Silmi Rahma Amelia − *Master Program in Computational Science, Faculty of Mathematics and Natural Sciences, Institut Teknologi Bandung, Bandung, West Java 40132, Indonesia*

Citra Deliana Dewi Sundari − *Department of Chemistry, Institut Teknologi Bandung, Bandung, West Java 40132, Indonesia; Chemistry Education, Universitas Islam Negeri Sunan Gunung Djati Bandung, Bandung, West Java 40614, Indonesia;* orcid.org/0000-0002-0106-276X

Heni Rachmawati − *School of Pharmacy and Research Center for Nanosciences and Nanotechnology, Institut Teknologi Bandung, Bandung, West Java 40132, Indonesia*

Complete contact information is available at: https://pubs.acs.org/10.1021/acsomega.4c00759

Notes

The authors declare no competing financial interest.

ACKNOWLEDGMENTS

This work was fully supported by the Indonesian Endowment Fund for Education and the Indonesian Science Fund through the International Collaboration RISPRO Funding Program (Grant No. RISPRO/KI/B1/KOM/11/4542/2/2020).

REFERENCES

(1) World Health Organization (WHO). *Novel Coronavirus (2019-nCoV): Situation Report − 1*; 2020 (accessed January 2022).

(2) Oran, D. P.; Topol, E. J. Prevalence of Asymptomatic SARS-CoV-2 Infection. *Ann. Int. Med.* **2020**, *173*, 362−367, DOI: 10.7326/M20-3012.

(3) World Health Organization. *Knowing the risks for COVID-19*; 2020 (accessed January 2022).

(4) Wunsch, H. Mechanical Ventilation in COVID-19: Interpreting the Current Epidemiology. *Am. J. Respir. Crit. Care Med.* **2020**, *202*, 1−4, DOI: 10.1164/rccm.202004-1385ED.
(5) Barbaro, R. P.; MacLaren, G.; Boonstra, P. S.; Combes, A.; Agerstrand, C.; Annich, G.; Diaz, R.; Fan, E.; Hryniewicz, K.; Lorusso, R.; Paden, M. L.; Stead, C. M.; Swol, J.; Iwashyna, T. J.; Slutsky, A. S.; Brodie, D. Extracorporeal Life Support Organization. *Extracorporeal membrane oxygenation for COVID-19: evolving outcomes from the international Extracorporeal Life Support Organization Registry. Lancet* **2021**, *398* (10307), 1230−1238.
(6) Korber, B.; Fischer, W. M.; Gnanakaran, S.; Yoon, H.; Theiler, J.; Abfalterer, W.; Hengartner, N.; Giorgi, E. E.; Bhattacharya, T.; Foley, B.; Hastie, K. M.; Parker, M. D.; Partidge, D. G.; Evans, C. M.; Freeman, T. M.; de Silva, T. I.; Sheffield COVID-19 Genomics Group. Tracking Changes in SARS-CoV-2 Spike: Evidence that D614G Increases Infectivity of the COVID-19 Virus. *Cell* **2020**, *182* (4), 812−827.
(7) Banoun, H. Evolution of SARS-CoV-2: Review of Mutations, Role of the Host Immune System. *Nephron* **2021**, *145* (4), 392−403.
(8) Zhang, L.; Li, Q.; Liang, Z.; Li, T.; Liu, S.; Cui, Q.; Nie, J.; Wu, Q.; Qu, X.; Huang, W.; Wang, Y. The significant immune escape of pseudotyped SARS-CoV-2 variant Omicron. *Emerging Microbes & Infections* **2022**, *11* (1), 1−5.
(9) World Health Organization. *Classification of Omicron (B.1.1.529): SARS-CoV-2 Variant of Concern*; 2021 (accessed January 2022).
(10) Wolter, N.; Jassat, W. S.; Welch, R.; Moultrie, H.; Groome, M.; Amoako, D. G.; Everatt, J.; Bhiman, J. N.; Scheepers, C.; Tebeila, N.; Chiwandire, N.; Du Plessis, M.; Govender, N.; Ismail, A.; Glass, A.; Mlisana, K.; Stevens, W.; Treurnicht, F. K.; Makatini, Z.; Hsiao, N.; Parboosing, R.; Wadula, J.; Hussey, H.; Davies, M.; Boulle, A.; Gottberg, A.; Cohen, C. Early assessment of the clinical severity of the SARS-CoV-2 omicron variant in South Africa: a data linkage study. *Lancet* **2022**, *399*, 437−446, DOI: 10.1016/S0140-6736(22)00017-4.
(11) Saxena, S. K.; Kumar, S.; Ansari, S.; Paweska, J. T.; Maurya, V. K.; Tripathi, A. K.; Abdel-Moneim, A. S. Characterization of the novel SARS-CoV-2 Omicron (B.1.1.529) variant of concern and its global perspective. *J. Med. Virol.* **2022**, *94*, 1738−1744, DOI: 10.1002/jmv.27524.
(12) Ortega, J. T.; Jastrzebska, B.; Rangel, H. R. Omicron SARS-CoV-2 Variant Spike Protein Shows an Increased Affinity to the Human ACE2 Receptor: An In Silico Analysis. *Pathogens* **2022**, *11*, 45.
(13) Tai, W.; He, L.; Zhang, X.; Pu, J.; Voronin, D.; Jiang, S.; Du, L. Characterization of the receptor-binding domain (RBD) of 2019 novel coronavirus: implication for development of RBD protein as a viral attachment inhibitor and vaccine. *Cell. Mol. Immunol.* **2020**, *17*, 613−620, DOI: 10.1038/s41423-020-0400-4.
(14) Zhang, H.; Penninger, J. M.; Li, Y.; Zhong, N.; Slutsky, A. S. Angiotensin-converting enzyme 2 (ACE2) as a SARS-CoV-2 receptor: molecular mechanisms and potential therapeutic target. *Intensive Care Med.* **2020**, *46*, 586−590, DOI: 10.1007/s00134-020-05985-9.
(15) Salamanna, F.; Maglio, M.; Landini, M. P.; Fini, M. Body Localization of ACE-2: On the Trail of the Keyhole of SARS-CoV-2. *Front. Med.* **2020**, *7*, No. 594495.
(16) Mathieu, E.; Ritchie, H.; Rodés-Guirao, L.; Appel, C.; Gavrilov, D.; Giattino, C.; Hasell, J.; Macdonald, B.; Dattani, S.; Beltekian, D.; Ortiz-Ospina, E.; Roser, M. *Corona Virus Pandemic (COVID-19)*; 2020. https://ourworldindata.org/coronavirus/ (accessed January 2022).
(17) Gugus Tugas percepatan Pelayanan Covid. *Informasi COVID − 19*; **2022**. https://data.covid19.go.id/public/index.html (accessed January 2022).
(18) Rella, S. A.; Kulikova, Y. A.; Dermitzakis, E. T.; Kondrashov, F. A. Rates of SARS-CoV-2 transmission and vaccination impact the fate of vaccine-resistant strains. *Sci. Rep.* **2022**, *11* (1), No. 15729, DOI: 10.1038/s41598-021-95025-3.
(19) Uzunova, K.; Filipova, E.; Pavlova, V.; Vekov, T. Insights into antiviral mechanisms of remdesivir, lopinavir/ritonavir and chloroquine/hydroxychloroquine affecting the new SARS-CoV-2. *Biomedicine & Pharmacotherapy* **2020**, *131*, No. 110668.
(20) Janik, E.; Niemcewicz, M.; Podogrocki, M.; Saluk-Bijak, J.; Bijak, M. Existing Drugs Considered as Promising in COVID-19 Therapy. *Int. J. Mol. Sci.* **2021**, *22*, 5434.
(21) Gordon, C. J.; Tchesnokov, E. P.; Woolner, E.; Perry, J. K.; Feng, J. Y.; Porter, D. P.; Götte, M. Remdesivir is a direct-acting antiviral that inhibits RNA-dependent RNA polymerase from severe acute respiratory syndrome coronavirus 2 with high potency. *J. Biol. Chem.* **2020**, *295*, 6785−6797, DOI: 10.1074/jbc.RA120.013679.
(22) Devaux, C. A.; Rolain, J.-M.; Colson, P.; Raoult, D. New insights on the antiviral effects of chloroquine against coronavirus: what to expect for COVID-19? *Int. J. Antimicrob. Agents* **2020**, *55* (5), No. 105938.
(23) Wu, C.; Liu, Y.; Yang, Y.; Zhang, P.; Zhong, W.; Wang, Y.; Wang, Q.; Xu, Y.; Li, M.; Li, X.; Zheng, M.; Chen, L.; Li, H. Analysis of therapeutic targets for SARS-CoV-2 and discovery of potential drugs by computational methods. *Acta Pharm. Sin. B* **2020**, *10*, 766−788, DOI: 10.1016/j.apsb.2020.02.008.
(24) Goldman, J. D.; Lye, D. C. B.; Hui, D. S.; Marks, K. M.; Bruno, R.; Montejano, R.; Spinner, C. D.; Galli, M.; Ahn, M. Y.; Nahass, R. G.; Chen, Y. S.; SenGupta, D.; Hyland, R. H.; Osinusi, A. O.; Cao, H.; Blair, C.; Wei, X.; Gaggar, A.; Brainard, D. M.; Towner, W. J.; Muñoz, J.; Mullane, K. M.; Marty, F. M.; Tashima, K. T.; Diaz, G.; Subramanian, A. GS-US-540-5773 Investigators Remdesivir for 5 or 10 days in patients with severe Covid-19. *N. Engl. J. Med.* **2020**, *383* (19), 1827−1837.
(25) Gevers, S.; Kwa, M. S. G.; Wijnans, E.; van Nieuwkoop, C. Safety considerations of chloroquine and hydroxychloroquine in treatment of COVID-19. *Clin. Microbiol. Infect.* **2020**, *26*, 1276−1277, DOI: 10.1016/j.cmi.2020.05.006.
(26) Owa, A. B.; Owa, O. T. Lopinavir/ritonavir use in Covid-19 infection: is it completely non-beneficial? *J. Microbiol., Immunol. Infect.* **2020**, *53*, 674−675, DOI: 10.1016/j.jmii.2020.05.014.
(27) Kasálková, N. S.; Slepička, P.; Švorčík, V. Carbon Nanostructures, Nanolayers, and Their Composites. *Nanomaterials* **2021**, *11* (9), 2368.
(28) Rauti, R.; Musto, M.; Bosi, S.; Prato, M.; Ballerini, L. Properties and behavior of carbon nanomaterials when interfacing neuronal cells: how far have we come? *Carbon* **2019**, *143*, 430−446, DOI: 10.1016/j.carbon.2018.11.026.
(29) Zhu, S.; Yan, X.; Liu, J. R. A.; Zhu, Q. Old Story New Tell: The Graphite to Diamond Transition Revisited. *Condens. Matter* **2020**, *3*, 864−878, DOI: 10.1016/j.matt.2020.05.013.
(30) Tiwari, S. K.; Sahoo, S.; Wang, N.; Huczko, A. Graphene Research and their Outputs: Status and Prospect. *J. Sci.: Adv. Mater. Devices* **2020**, *5*, 10−29, DOI: 10.1016/j.jsamd.2020.01.006.
(31) Tian, P.; Tang, L.; Teng, K. S.; Lau, S. P. Graphene quantum dots from chemistry to applications. *Materials Today Chemistry* **2018**, *10*, 221−258.
(32) Bressi, V.; Ferlazzo, A.; Iannazzo, D.; Espro, C. Graphene Quantum Dots by Eco-Friendly Green Synthesis for Electrochemical Sensing: Recent Advances and Future Perspectives. *Nanomaterials* **2021**, *11* (5), 1120.
(33) Dong, J.; Wang, K.; Sun, L.; Sun, B.; Yang, M.; Chen, H.; Dong, L. Application of graphene quantum dots for simultaneous fluorescence imaging and tumor-targeted drug delivery. *Sens. Actuators, B* **2018**, *256*, 616−623.
(34) Chen, F.; Gao, W.; Qiu, X.; Zhang, H.; Liu, L.; Liao, P.; Luo, Y. Graphene quantum dots in biomedical applications: Recent advances and future challenges. *Front. Lab. Med.* **2017**, *1* (4), 192−199.
(35) Ghosh, D.; Sarkar, K.; Devi, P.; Kim, K.-H.; Kumar, P. Current and future perspectives of carbon and graphene quantum dots: From synthesis to strategy for building optoelectronic and energy devices. *Renewable and Sustainable Energy Reviews* **2021**, *135*, No. 110391.

(36) Vallianou, N. G.; Evangelopoulos, A.; Schizas, N.; Kazazis, C. Potential anticancer properties and mechanisms of action of curcumin. *Anticancer Res.* **2015**, *35* (2), 645−651.
(37) Lin, C.; Chang, L.; Chu, H.; Lin, H.; Chang, P.; Wang, R. Y. L.; Unnikrishnan, B.; Mao, J.; Chen, S.; Huang, C. High Amplification of the Antiviral Activity of Curcumin through Transformation into Carbon Quantum Dots. *Small* **2019**, No. e1902641.
(38) Chen, H.; Lin, C.; Anand, A.; Lin, H.; Lin, H.; Mao, J.; Wang, P.; Tseng, Y. J.; Tzou, W.; Huang, C.; Wang, R. Y. L. Development of Antiviral Carbon Quantum Dots that Target the Japanese Encephalitis Virus Envelope Protein. *J. Biol. Chem.* **2022**, *298* (6), No. 101957.
(39) RSCB Protein Data Bank. *Crystal Structure of SARS-CoV-2 Spike Receptor-Binding Domain Bound with ACE2*; 2020. https://www.rcsb.org/structure/6M0J.
(40) Pubchem. *Curcumin*; 2022. https://pubchem.ncbi.nlm.nih.gov/compound/Curcumin.
(41) Hanwell, M. D.; Curtis, D. E.; Lonie, D. C.; Vandermeersch, T.; Zurek, E.; Hutchison, G. R. Avogadro: An advanced semantic chemical editor, visualization, and analysis platform. *J. Cheminform.* **2012**, *4*, 17.
(42) Land, H.; Humble, M. S. YASARA: A Tool to Obtain Structural Guidance in Biocatalytic Investigations. *Protein Eng.* **2018**, *1685*, 43−67.
(43) Neese, F. The ORCA program system. *Wiley Interdisciplinary Reviews: Computational Molecular Science* **2012**, *2* (1), 73−78.
(44) Neese, F. Software update: the ORCA program system, version 4.0. *Wiley Interdiscip. Rev.: Comput. Mol. Sci.* **2018**, *8* (1), No. e1327.
(45) Kohn, W.; Sham, L. J. Self-Consistent Equations Including Exchange and Correlation Effects. *Phys. Rev.* **1965**, *140* (4A), A1133−A1138.
(46) Becke, A. D. Density-functional exchange-energy approximation with correct asymptotic behavior. *Phys. Rev. A* **1988**, *38*, 3098−3100.
(47) Lee, C.; Yang, W.; Parr, R. G. Development of the Colle−Salvetti correlation-energy formula into a functional of the electron density. *Phys. Rev. B* **1988**, *37*, 785−789.
(48) Weigend, F.; Ahlrichs, R. Balanced basis sets of split valences, triple zeta valence and quadruple zeta valence quality for H to Rn: Design and assessment of accuracy. *Phys. Chem. Chem. Phys.* **2005**, *7* (18), 3297.
(49) Tsuneda, T.; Song, J.-W.; Suzuki, S.; Hirao, K. On Koopmans' theorem in density functional theory. *J. Chem. Phys.* **2010**, *133* (17), No. 174101.
(50) Bulat, F. A.; Chamorro, E.; Fuentealba, P.; Toro-Labbé, A. Condensation of Frontier Molecular Orbital Fukui Functions. *J. Phys. Chem. A* **2004**, *108* (2), 342−349.
(51) Johnson, E. R.; Keinan, S.; Mori-Sánchez, P.; Contreras-García, J.; Cohen, A. J.; Yang, W. Revealing Noncovalent Interactions. *J. Am. Chem. Soc.* **2010**, *132* (18), 6498−6506.
(52) Humphrey, W.; Dalke, A.; Schulten, K. VMD: Visual molecular dynamics. *J. Mol. Graphics* **1996**, *14* (1), 33−38.
(53) Glendening, E. D.; Landis, C. R.; Weinhold, F. NBO 7.0: New vistas in localized and delocalized chemical bonding theory. *J. Comput. Chem.* **2019**, *40*, 2234−2241.
(54) Fukui, K.; Yonezawa, T.; Shingu, H. A Molecular Orbital Theory of Reactivity in Aromatic Hydrocarbons. *J. Chem. Phys.* **1952**, *20* (4), 722−725.
(55) Miar, M.; Shiroudi, A.; Pourshamsian, K.; Oliaey, A. R.; Hatamjafari, F. Theoretical investigations on the HOMO−LUMO gap and global reactivity descriptor studies, natural bond orbital, and nucleus-independent chemical shifts analyses of 3-phenylbenzo[d]-thiazole-2(3H)-imine and its para-substituted derivatives: Solvent and substituent effects. *J. Chem. Res.* **2021**, *45*, 147−158.
(56) Ghahremanian, S.; Rashidi, M. M.; Raeisi, K.; Toghraie, D. Molecular dynamics simulation approach for discovering potential inhibitors against SARS-CoV-2: A structural review. *J. Mol. Liq.* **2022**, *354*, No. 118901.
(57) Rahma, M. M.; Saha, T.; Islam, K. J.; Suman, R. H.; Biswas, S.; Rahat, E. U.; Hossen, M. R.; Islam, R.; Hossain, M. N.; Mamun, A. A.; Khan, M.; Ali, M. A.; Halim, M. A. Virtual screening, molecular dynamics and structure−activity relationship studies to identify potent approved drugs for Covid-19 treatment. *J. Biomol. Struct. Dyn.* **2020**, *39*, 6231−6241.

https://doi.org/10.1021/acsomega.4c00759
ACS Omega 2024, 9, 16701−16715